Combined effect of resistance spot welding and precipitation hardening on tensile shear load bearing capacity of A286 superalloy

Óscar Martín[a,*], Pilar De Tiedra[b], Manuel San-Juan[a]

[a] Ingeniería de los Procesos de Fabricación, Departamento CMeIM/EGI/ICGF/IM/IPF, Universidad de Valladolid, Escuela de Ingenierías Industriales, Paseo del Cauce 59, Valladolid 47011, Spain.

[b] Ciencia de los Materiales e Ingeniería Metalúrgica, Departamento CMeIM/EGI/ICGF/IM/IPF, Universidad de Valladolid, Escuela de Ingenierías Industriales, Paseo del Cauce 59, Valladolid 47011, Spain.

* Corresponding author. Ph.: +34-983423533, Fax: +34-983423310, E-mail: oml@eii.uva.es (Ó. Martín)

Abstract

This work aims to study the combined effect of resistance spot welding (RSW) and precipitation hardening on tensile shear load bearing capacity (TSLBC) of A286 superalloy. The tensile shear test specimens were welded in the solution treated condition, and then subjected to different precipitation hardening treatments. The impoverishment in Ti, due to its segregation towards the interdendritic region (studied by performing SEM/EDX analysis), causes the development of gamma prime depleted zones in the dendrite core of the weld nugget, which is associated with a decrease of the mechanical properties with respect to the base metal. The segregation of Ti towards the interdendritic region of the weld nugget has also influence on the eta phase formation, which appears later (with longer aging times) in the weld nugget than in the base metal. The aging time at which the maximum experimental TSLBC is reached is, for both aging temperatures, 100 h. The experimental TSLBC of the tensile shear test specimens hardened at lower aging temperature is greater (except for the shortest aging time) than that of those hardened at higher aging temperature.

Keywords: Resistance spot welding; A286 superalloy; Precipitation hardening; gamma prime phase; eta phase; tensile shear load bearing capacity.

1 Introduction

A286 iron-nickel superalloy is a precipitation-hardenable austenitic stainless steel which, as indicated by Mustafa et al. [1], is extensively used in gas turbine industry due to its good thermal resistance and superior mechanical properties, with several advantages over nickel or cobalt superalloys such as a lower thermal expansion at high temperature, which is an important property for engine components requiring closely controlled clearances between rotating parts, and a lower cost [2]. A286 superalloy is also utilized in cryogenic devices [3], in nonmagnetic oil well equipments [3], and in the nuclear industry [4,5].

A286 superalloy is strengthened by the precipitation of the ordered fcc gamma prime (γ') $Ni_3(Al,Ti)$ phase [6–8], which, as pointed out by Zhao et al. [9] and by Zhang et al. [10], is coherent with the matrix. Since, the γ' phase is unstable [11], after a sufficiently long aging treatment at sufficiently high temperature, dissolves to form the hcp eta (η) Ni_3Ti phase that, at aging temperatures between 600 and 850 °C [12], precipitates at grain boundary by cellular reaction [13].

The cellular η phase precipitation at grain boundary may be detrimental to the mechanical properties because degrades the creep behaviour [14], causes the increase in intergranular fracture in the tensile test [15], aggravates the hydrogen embrittlement sensitivity [16], and induces the decrease in fatigue life [17].

A286 superalloy is a difficult material to weld due to its high susceptibility to hot cracking in the fusion zone [18]; this solidification cracking is caused by the formation of a low melting point phase at the grain boundaries, which is produced by the segregation of titanium and other solutes during the last stages of solidification [19–21].

Resistance spot welding (RSW) is one of the primary methods to join sheet metals in the automotive industry [22–25], due to the fact that, as stated by Khodabakhshi et al. [26], it has the highest throughput. RSW of stainless steel sheets is also extensively used, as mentioned by Kianersi at al. [27], in transportation vessels, kitchen furniture and utensils and building applications. Although the general practice in welding superalloys is to employ a weaker, more ductile austenitic filler metal than the base metal to minimize weld cracking, when the maximum joint strength is required, filler metal of base metal composition is used [28]. Therefore, RSW, which is an autogenous welding process (i.e., without filler metal), may be a promising method for welding A286 superalloy. On the other hand, RSW may be used for welding dissimilar metals [29,30], which is a matter of great interest due to its technical and economical potentials [31].

Structures employing RSW joints are usually designed so that these joints are loaded in shear when the parts are exposed to tension or compression loading [32]; and static tensile shear test is, according to Zhou et al. [33], the most common laboratory test used in the determination of weld strength due to its simplicity. Therefore, the quality of the RSW joints may be assessed from its tensile shear load bearing capacity (TSLBC), which is the peak load value obtained during the tensile shear test [34,35].

In the present work, the TSLBC of several RSW joints of A286 superalloy, which were welded in the solution treated condition and then subjected to different precipitation hardening treatments, were obtained and analysed in light of the different formation kinetics of γ' and η precipitates in the weld nugget with respect to that observed in the base metal.

2 Experimental Procedure

2.1 Materials

The chemical composition of the A286 superalloy sheets welded by RSW is shown in Table 1. The sheet thickness was 1 mm.

Table 1. Chemical composition of A286 superalloy sheets (wt %).

C	Si	Mn	P	S	Cr	Mo	Ni	V	Ti	Al	B	Fe
0.032	0.50	1.24	0.011	<0.0003	14.98	1.18	24.74	0.29	2.30	0.16	0.0046	Bal.

2.2 Scanning Electron Microscope (SEM)

SEM micrographs were obtained after mechanical polishing and electrolytic etching with etchant No. 83 according to ASTM E407-07e1 (at 6 V for 60 s in a solution of 10 g CrO_3 in 100 ml water) [36]. SEM observations were conducted on a FEI-Quanta 200FEG operating at 20 kV and equipped with an energy dispersive X-ray analysis (EDX) to determine the chemical composition of interdendritic region.

2.3 Tensile shear tests

Tensile shear tests were performed, on a Shimadzu UH-F500 kNA universal testing machine, at a crosshead speed of 2 mm/min which, according to Marashi et al. [37], allows to consider the test as static. The tensile shear test specimens were prepared according to ISO 14273 [38], and were welded, as recommended by Hoppin and Yount [28], in the solution treated condition (solution treatment was carried out at 927 °C for 0.25 h and followed by water quenching), and then subjected to different precipitation hardening treatments (see Table 2). According to Table 2, there were 13 different tensile shear test specimens.

The A286 superalloy sheets were welded with a single-phase alternating current (AC) 50 Hz equipment by using water-cooled truncated cone RWMA Group A Class 2 electrodes [39] with 16 mm body diameter and 5 mm face diameter. The controlled parameters in the RSW process of the tensile shear test specimens were, according to Aslanlar [40]: welding time (WT), welding current (WC), and electrode force (EF). The values of the welding parameters were fixed at WT = 0.36 s, WC = 6 kA and EF = 2300 N [19].

Table 2. Tensile shear test specimens. Specimen No. 0 was subjected to no precipitation hardening treatment, i.e. it was in the solution treated condition. Each of different precipitation hardening treatments was followed by air cooling.

Solution treated condition		RSW process	Precipitation hardening		Specimen No.
Temperature (°C)	Time (h)		Temperature (°C)	Time (h)	
927	0.25	WT = 0.36 s WC = 6 kA EF = 2300 N	N/A	N/A	0
			670	0.5	1
				10	2
				25	3
				50	4
				100	5
				200	6
			720	0.5	7
				10	8
				25	9
				50	10
				100	11
				200	12

2.4 Vickers microhardness

The Vickers microhardness was measured across the cross sectioned RSW joint using a Matsuzawa Seiki MXT 70 Vickers microhardness tester with a load of 500g.

3 Results and discussion

The most important factor affecting TSLBC is, according to Hasanbaşoğlu and Kaçar [41] and Kong et al. [42] the size of weld nugget, which, as pointed out by Raoelison et al. [43], is formed from the solidification of the molten metal after a heating by Joule effect and, consequently, has an as-cast dendritic microstructure (Fig.1).

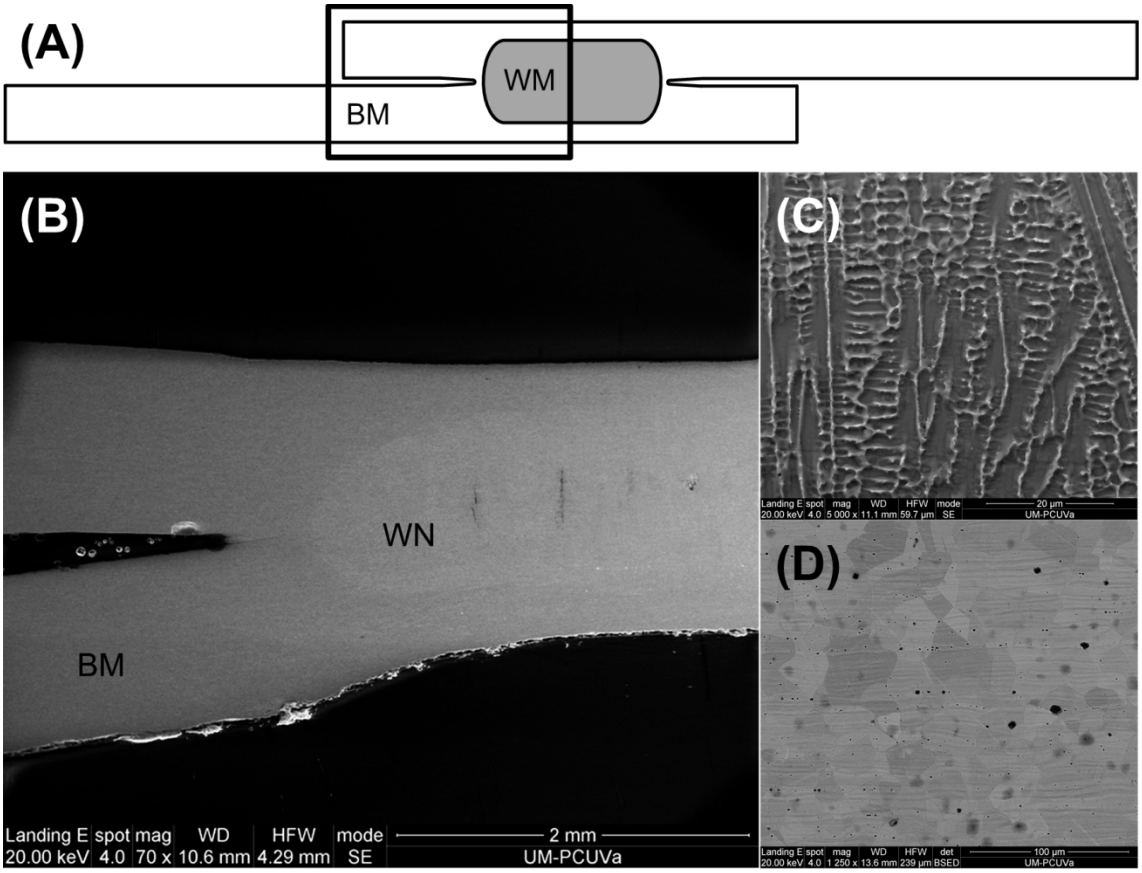

Fig. 1. (A) Diagram (not to scale) that shows the location of the area where the micrograph (B) was taken from the tensile shear test specimen; (B) SEM micrograph of a cross sectioned tensile shear test specimen that shows the weld nugget (WN) and the base metal (BM); (C) SEM micrograph of the as-cast dendritic microstructure of the weld nugget; (D) SEM micrograph of the base metal, which has polygonal austenitic grains. Electrolytic etching with etchant No. 83 according to ASTM E407-07 [36].

The experimental TSLBC, which was obtained in the tensile shear test (Fig. 2), and the predicted TSLBC, which was used as a reference, of each of the 13 tensile shear test specimens are shown in Fig. 3. The predicted TSLBC was obtained from Eq. (1) [44,45]:

$$P = 10^{-3} \cdot f \cdot t \cdot d \cdot \sigma_R \tag{1}$$

where P is the predicted TSLBC (kN); f is a coefficient whose value was taken as 2.65; t is the sheet thickness (1 mm); d is the weld nugget diameter whose value was taken as 5.5 mm; and

σ_R is the tensile strength (MPa) of the base metal whose value was taken from previous work by De Tiedra et al. [46].

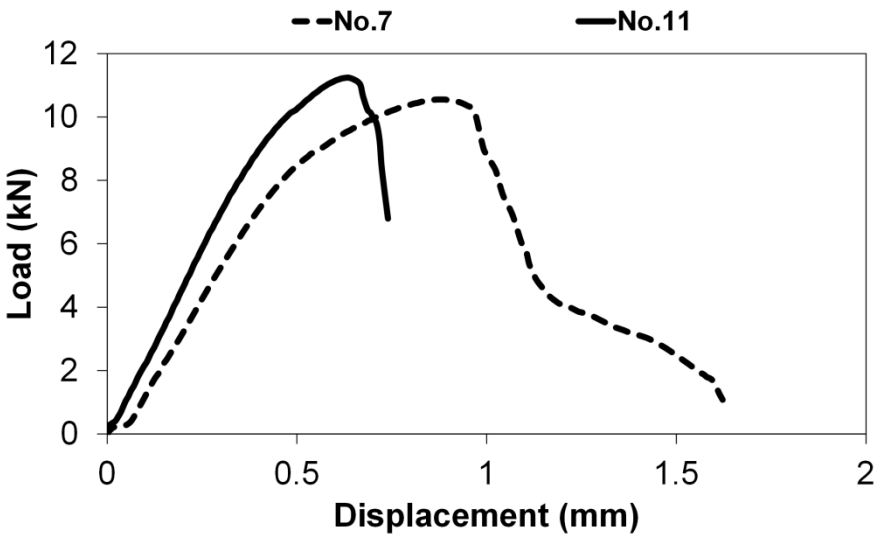

Fig. 2. Load vs. displacement curves obtained from the tensile shear test performed on specimen No. 7 (precipitation hardening carried out at 720 °C for 0.5 h) and specimen No. 11 (precipitation hardening carried out at 720 °C for 100 h).

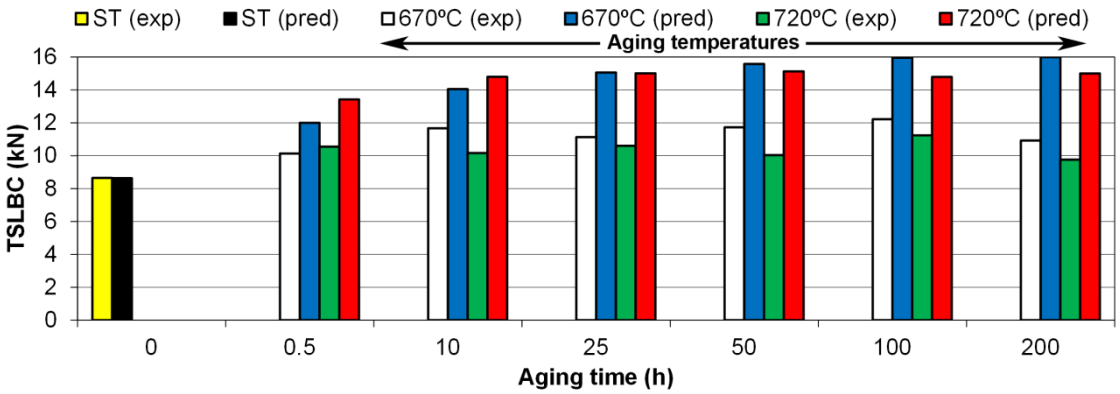

Fig. 3. Experimental (exp) TSLBC, which was obtained in the tensile shear test, and predicted (pred) TSLBC [44,45] of each of the 13 tensile shear test specimens. Specimen No. 0 was subjected to no precipitation hardening treatment, i.e. it was in the solution treated (ST) condition and its aging time was considered as 0 h.

As shown in Fig. 3, the experimental and predicted values of TSLBC coincide for the specimen that was subjected to no precipitation hardening treatment, but in all other cases the value of the experimental TSLBC is less than that of the predicted TSLBC, which may be explained by the fact that the predicted TSLBC does not fully capture the effect of precipitation hardening treatment on the as-cast dendritic microstructure of the weld nugget, whereas this effect is indeed captured by the experimental TSLBC.

The interdendritic regions of the weld nugget microstructure are enriched in certain solute elements whose segregation occurs during the solidification [19–21]. This phenomenon was studied by performing SEM/EDX analysis on the interdendritic region of the weld nugget (Figs. 4 and 5). The main results of this analysis are shown in Table 3.

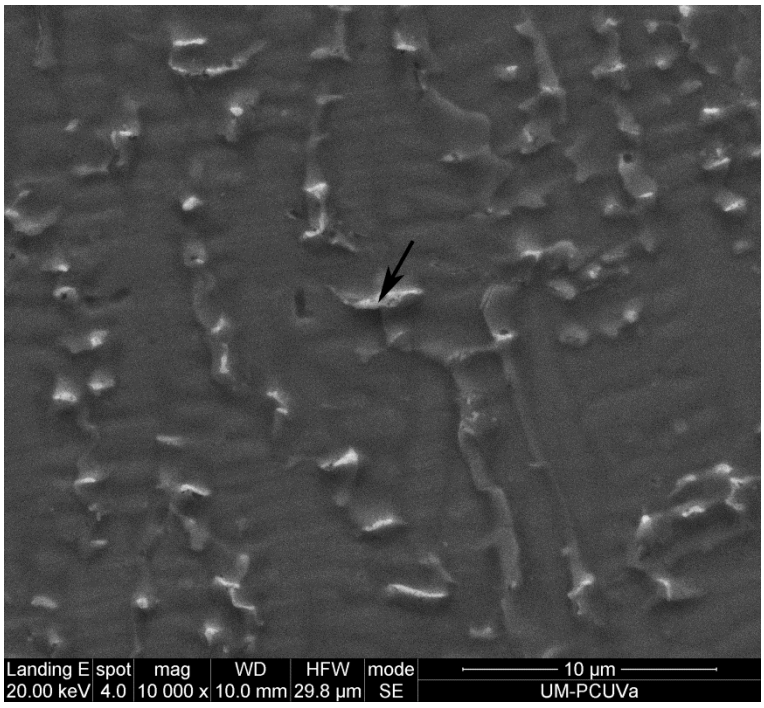

Fig. 4. SEM micrograph of the weld nugget of the tensile shear test specimen No. 5. The arrow indicates the interdendritic region where the SEM/EDX analysis was performed. Electrolytic etching with etchant No. 83 according to ASTM E407-07 [36].

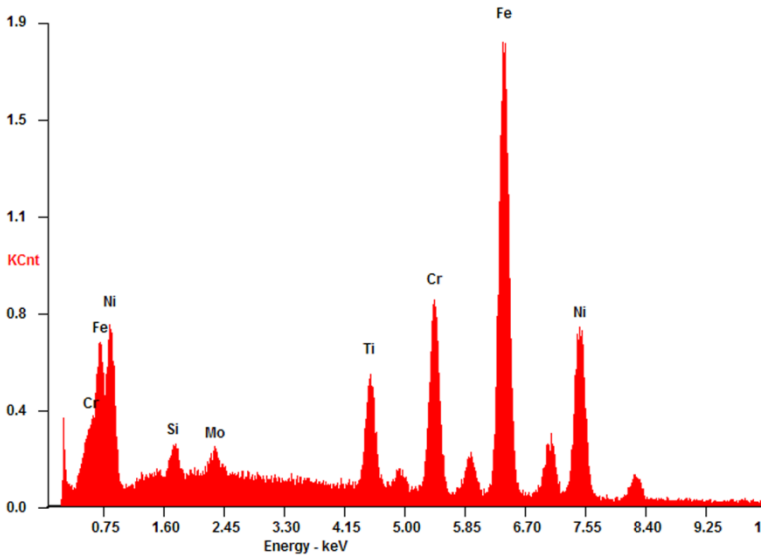

Fig. 5. EDX spectrum obtained from the interdendritic región shown in Fig. 4.

As shown in Table 3, the interdendritic region of the weld nugget is enriched, according to the ratio *k* between the interdendritic region composition and the nominal composition of the alloy [18], in Ni, Mo and especially in Ti and Si; this result agrees with that obtained by Brooks and Krenzer [21].

Table 3. Chemical composition (wt%) of interdendritic region determined by EDX and ratio k.

Element	wt%	k
Si	1.4	2.8
Mo	02.43	2.06
Ti	05.92	2.57
Cr	13.25	0.88
Fe	47.8	0.88
Ni	29.20	1.18

Although the segregation of Si and Ti towards the interdendritic region of the weld nugget may give rise to the formation of low melting point eutectics associated with the hot cracking [21,47], the most significant result is the influence of the impoverishment in Ti of the dendrite core (due to the enrichment of the interdendritic region) on the formation of two important Ti-rich phases: (i) the strengthening γ' phase; and (ii) the η phase, which may be detrimental to the mechanical properties.

The impoverishment in Ti causes the development of γ' depleted zones in the dendrite core of the weld nugget (Fig. 6), which is associated with a decrease of the mechanical properties with respect to the base metal [18] (Figs. 7 and 8). This drawback may be addressed, as suggested by Chen et al. [18], by increasing the nominal Ti content in the iron-nickel superalloy (base metal), which would give rise to better mechanical properties due to the uniform distribution of γ' precipitates in the weld nugget.

The segregation of Ti towards the interdendritic region of the weld nugget has also influence on the η phase formation, which appears later (with longer aging times) in the weld nugget than in the base metal. In the base metal, at 720 °C, 25 h is the aging time from which there is evidence of the presence of η phase (Fig. 9) and at 670 °C, 100 h is the aging time from which there is evidence of the presence of η phase [46,48] (Fig. 10), whereas, in the weld nugget, at 720 °C, 50 h is the aging time from which there is evidence of the presence of η phase (Fig. 6) and at 670 °C, after an aging time of 200 h, there is no evidence of the presence of η phase (Fig. 11).

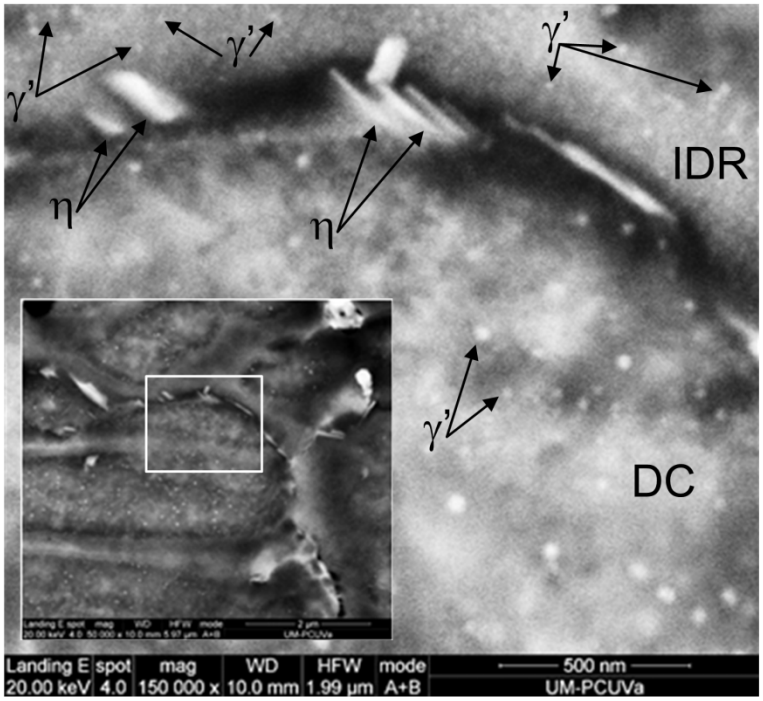

Fig. 6. SEM micrograph of the weld nugget of the tensile shear test specimen No. 10 where the inset provides the location of the studied zone. The γ' depleted zones in the dendrite core (DC) and the η phase at the interface between dendrite core and interdendritic region (IDR) are shown. Electrolytic etching with etchant No. 83 according to ASTM E407-07 [36].

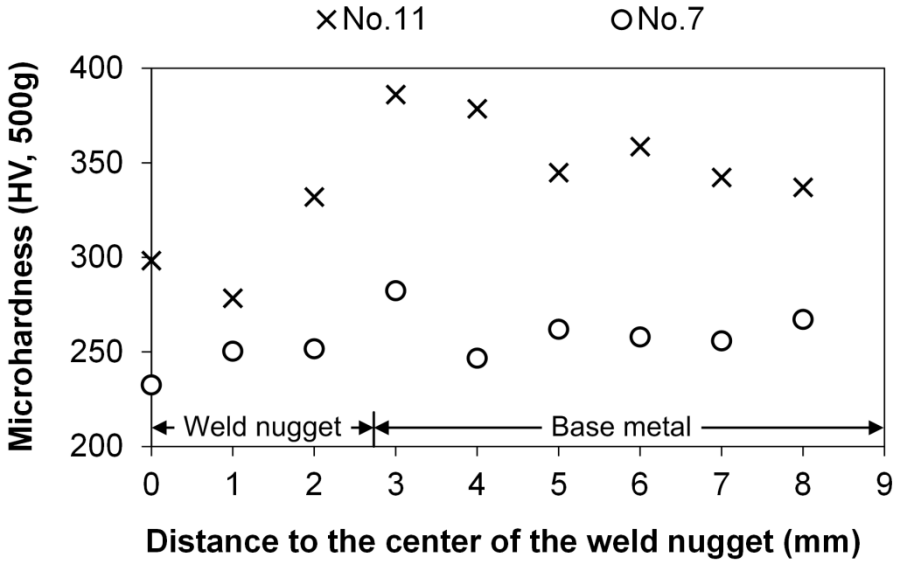

Fig. 7. Vickers hardness profile in the cross sectioned tensile shear test specimens No.7 and No. 11.

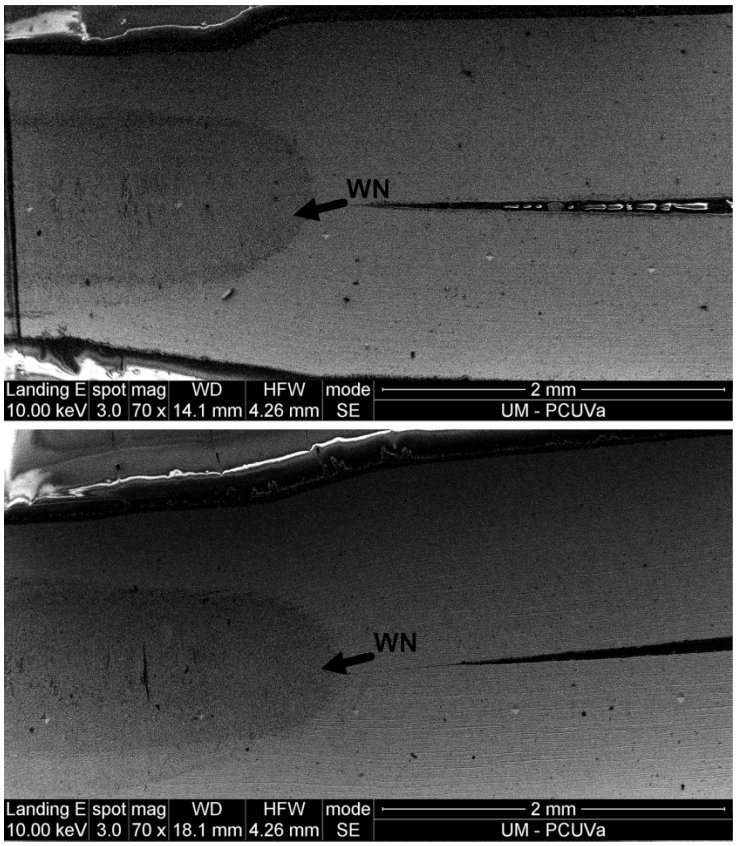

Fig. 8. SEM micrographs that show Vickers indentations [49], performed on the cross sectioned tensile shear test specimens No.7 (bottom) and No. 11 (top). Electrolytic etching with etchant No. 83 according to ASTM E407-07 [36].

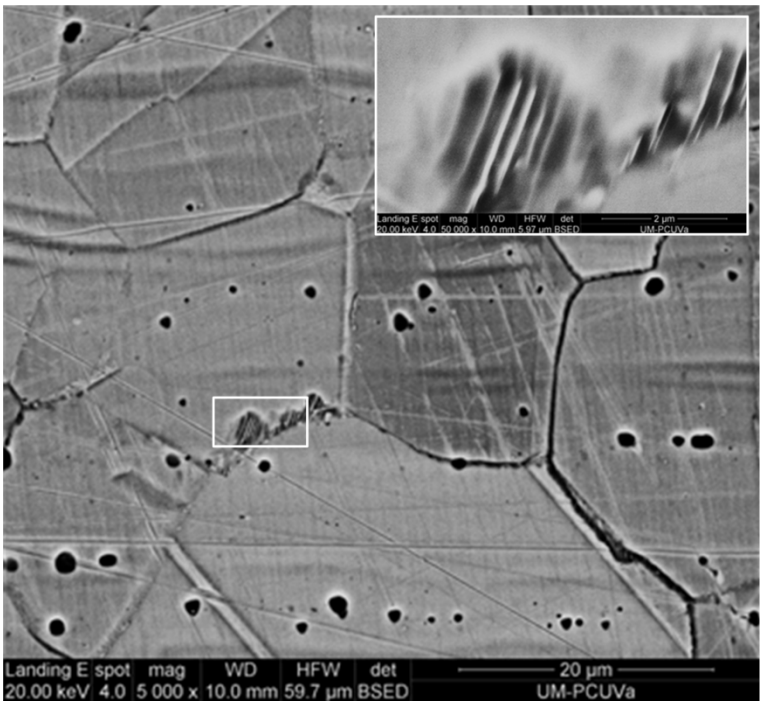

Fig. 9. SEM micrograph of the base metal of the tensile shear test specimen No. 9 that shows the η phase precipitation at grain boundary. The inset provides a higher magnification image of the η phase. Electrolytic etching with etchant No. 83 according to ASTM E407-07 [36].

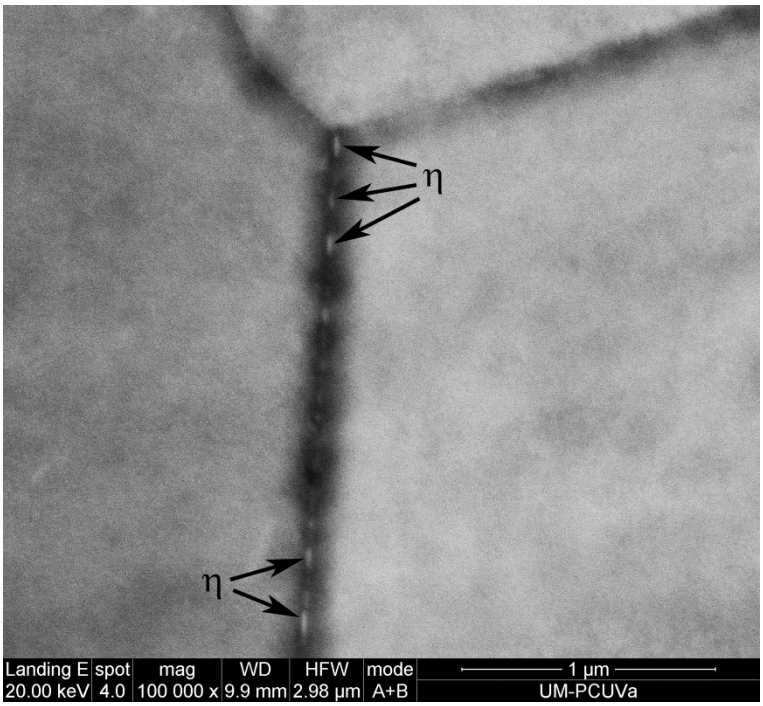

Fig. 10. SEM micrograph of the base metal of the tensile shear test specimen No. 5 that shows the η phase precipitation at grain boundary. Electrolytic etching with etchant No. 83 according to ASTM E407-07 [36].

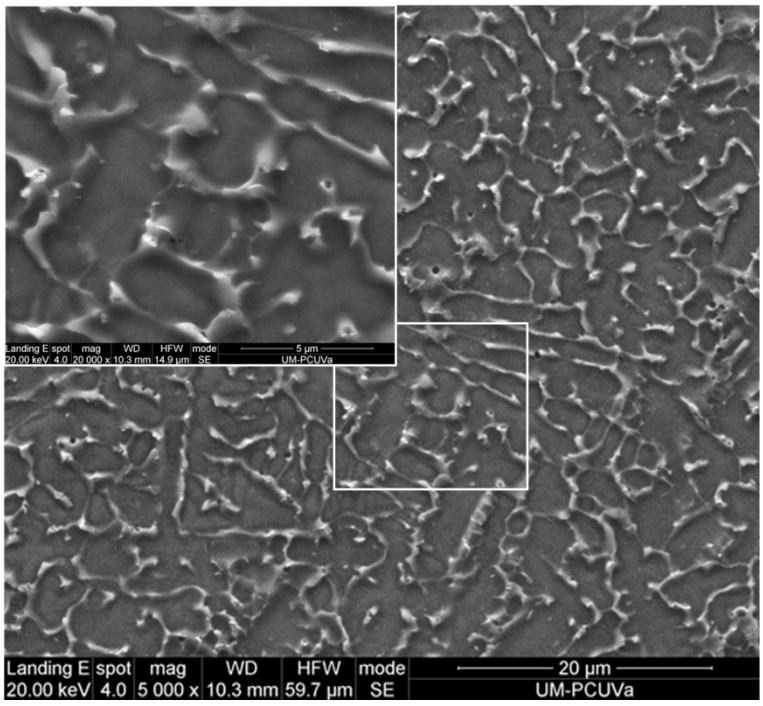

Fig. 11. SEM micrograph of the weld nugget of the tensile shear test specimen No. 6 where there is no evidence of the presence of η phase. The inset provides a higher magnification image of the selected zone. Electrolytic etching with etchant No. 83 according to ASTM E407-07 [36].

As shown in Fig. 3, the aging time at which the maximum experimental TSLBC is reached is, for both aging temperatures (670 and 720 °C), 100 h. This result may be explained by the fact that, as explained by Thompson and Brooks [8], γ' phase is precipitated early in aging and subsequent aging is basically a coarsening process where, as pointed out by several authors [50–52], strength increases with increasing γ' precipitate size until a maximum strength is reached. In addition to this, the η phase that, as demonstrated by Brooks and Thompson [15], causes the increase in intergranular fracture in the tensile test, and grows at the expense of γ' phase [11,53–55], appears in the weld nugget of the specimens subjected to precipitation hardening at 720 °C. Finally, the experimental TSLBC of the tensile shear test specimens hardened at lower aging temperature is greater (except for the shortest aging time) than that of those hardened at higher aging temperature, which may be explained by the fact that the growth kinetics of γ' precipitates is faster at higher aging temperatures [56].

4 Conclusions

This work aims to study the combined effect of RSW and precipitation hardening on TSLBC of A286 superalloy. The major conclusions are:

1. The impoverishment in Ti, due to its segregation towards the interdendritic region, causes the development of γ' depleted zones in the dendrite core of the weld nugget, which is associated with a decrease of the mechanical properties with respect to the base metal. This drawback may be addressed by increasing the nominal Ti content in the iron-nickel superalloy (base metal), which would give rise to better mechanical properties due to the uniform distribution of γ' precipitates in the weld nugget.
2. The segregation of Ti towards the interdendritic region of the weld nugget has also influence on the η phase formation, which appears later (with longer aging times) in the weld nugget than in the base metal.
3. The aging time at which the maximum experimental TSLBC is reached is, for both aging temperatures (670 and 720 °C), 100 h.
4. The experimental TSLBC of the tensile shear test specimens hardened at lower aging temperature is greater (except for the shortest aging time) than that of those hardened at higher aging temperature.

References

[1] A.H. Mustafa, M.S. Hashmi, B.S. Yilbas, M. Sunar, Investigation into thermal stresses in gas turbine transition-piece: Influence of material properties on stress levels, J. Mater. Process. Technol. 201 (2008) 369–373. doi:10.1016/j.jmatprotec.2007.11.264.

[2] A.P. Mouritz, Introduction to Aerospace Materials, Woodhead Publishing Limited, Cambridge, UK, 2012.

[3] M. Narayana Rao, High performance stainless steels for critical engineering applications, Trans. Indian Inst. Met. 63 (2010) 321–330. doi:10.1007/s12666-010-0043-8.

[4] M. Savoie, C. Esnouf, L. Fournier, D. Delafosse, Influence of ageing heat treatment on alloy A-286 microstructure and stress corrosion cracking behaviour in PWR primary water, J. Nucl. Mater. 360 (2007) 222–230. doi:10.1016/j.jnucmat.2006.10.003.

[5] L. Fournier, M. Savoie, D. Delafosse, Influence of localized deformation on A-286 austenitic stainless steel stress corrosion cracking in PWR primary water, J. Nucl. Mater. 366 (2007) 187–197. doi:10.1016/j.jnucmat.2007.01.001.

[6] S.C. Krishna, N.K. Gangwar, A.K. Jha, B. Pant, P.V. Venkitakrishnan, On the direct aging of iron based superalloy hot rolled plates, Mater. Sci. Eng. A. 648 (2015) 274–279. doi:10.1016/j.msea.2015.09.073.

[7] L.K. Singhal, J.W. Martin, The mechanism of tensile yield in an age-hardened steel containing γ′ (ordered Ni3Ti) precipitates, Acta Metall. 16 (1968) 947–953. doi:10.1016/0001-6160(68)90061-8.

[8] A.W. Thompson, J.A. Brooks, The mechanism of precipitation strengthening in an iron-base superalloy, Acta Metall. 30 (1982) 2197–2203. doi:10.1016/0001-6160(82)90140-7.

[9] M.J. Zhao, Z.F. Guo, H. Liang, L.J. Rong, Effect of boron on the microstructure, mechanical properties and hydrogen performance in a modified A286, Mater. Sci. Eng. A Struct. Mater. Prop. Microstruct. Process. 527 (2010) 5844–5851. doi:http://dx.doi.org/10.1016/j.msea.2010.05.070.

[10] P. Zhang, Q. Zhu, C. Hu, C. Wang, G. Chen, H. Qin, Cyclic deformation behavior of a nickel-base superalloy under fatigue loading, Mater. Des. 69 (2015) 12–21. doi:10.1016/j.matdes.2014.12.047.

[11] M. Seifollahi, S.H. Razavi, S. Kheirandish, S.M. Abbasi, The Mechanism of η Phase Precipitation in A286 Superalloy During Heat Treatment, J. Mater. Eng. Perform. 22 (2013) 3063–3069. doi:10.1007/s11665-013-0592-1.

[12] X. Li, J. Zhang, L. Rong, Y. Li, Cellular η phase precipitation and its effect on the tensile properties in an Fe-Ni-Cr alloy, Mater. Sci. Eng. A. 488 (2008) 547–553. doi:10.1016/j.msea.2007.11.039.

[13] C.Y. Barlow, B. Ralph, Observations of cellular transformation products in nickel-base superalloys, J. Mater. Sci. 14 (1979) 2500–2508. doi:10.1007/BF00737041.

[14] H. De Cicco, M.I. Luppo, L.M. Gribaudo, J. Ovejero-García, Microstructural development and creep behavior in A286 superalloy, Mater. Charact. 52 (2004) 85–92. doi:10.1016/j.matchar.2004.03.007.

[15] J.A. Brooks, A.W. Thompson, Microstructure and hydrogen effects on fracture in the alloy A-286, Metall. Trans. A. 24 (1993) 1983–1991. doi:10.1007/BF02666333.

[16] Z. Guo, H. Liang, M. Zhao, L. Rong, Effect of boron addition on hydrogen embrittlement sensitivity in Fe-Ni based alloys, Mater. Sci. Eng. A. 527 (2010) 6620–6625. doi:10.1016/j.msea.2010.06.073.

[17] B.S. Rho, S.W. Nam, X. Xie, The effect of test temperature on the intergranular cracking of Nb-A286 alloy in low cycle fatigue, J. Mater. Sci. 37 (2002) 203–209. doi:10.1023/A:1013147319646.

[18] S. Chen, M. Zhao, L. Rong, Effect of Ti content on the microstructure and mechanical properties of electron beam welds in Fe-Ni based alloys, Mater. Sci. Eng. A. 571 (2013) 33–37. doi:10.1016/j.msea.2013.02.001.

[19] ASM International Handbook Committee, Welding, in: J.R. Davies (Ed.), ASM Spec. Handbook. Stainl. Steels, ASM International, Materials Park, OH, 1994: pp. 340–401.

[20] K. Shinozaki, Welding and joining Fe and Ni-base superalloys, Weld. Int. 15 (2001) 593–610. doi:10.1080/09507110109549411.

[21] J.A. Brooks, R.W. Krenzer, Progress toward a more weldable A-286, Weld. J. 53 (1974) 242S–245S.

[22] O. Martín, M. López, F. Martín, Redes neuronales artificiales para la predicción de la calidad en soldadura por resistencia por puntos, Rev. Metal. 42 (2006) 345–353. doi:10.3989/revmetalm.2006.v42.i5.32.

[23] Ó. Martín, M. Pereda, J.I. Santos, J.M. Galán, Assessment of resistance spot welding quality based on ultrasonic testing and tree-based techniques, J. Mater. Process. Technol. 214 (2014) 2478–2487. doi:10.1016/j.jmatprotec.2014.05.021.

[24] N. Becker, J. Gilgert, E.J. Petit, Z. Azari, The effect of galvanizing on the mechanical resistance and fatigue toughness of a spot welded assembly made of AISI410 martensite, Mater. Sci. Eng. A. 596 (2014) 145–156. doi:10.1016/j.msea.2013.12.008.

[25] Ó. Martín, M. López, P. De Tiedra, M.S. Juan, Prediction of magnetic interference from resistance spot welding processes on implantable cardioverter-defibrillators, J. Mater. Process. Technol. 206 (2008) 256–262. doi:10.1016/j.jmatprotec.2007.12.021.

[26] F. Khodabakhshi, M. Kazeminezhad, A.H. Kokabi, Metallurgical characteristics and failure mode transition for dissimilar resistance spot welds between ultra-fine grained and coarse-grained low carbon steel sheets, Mater. Sci. Eng. A. 637 (2015) 12–22. doi:10.1016/j.msea.2015.04.019.

[27] D. Kianersi, A. Mostafaei, J. Mohammadi, Effect of welding current and time on the microstructure, mechanical characterizations, and fracture studies of resistance spot welding joints of AISI 316L austenitic stainless steel, Metall. Mater. Trans. A Phys. Metall. Mater. Sci. 45 (2014) 4423–4442. doi:10.1007/s11661-014-2421-z.

[28] G.S. Hoppin, R.E. Yount, Fusion welding of age-hardenable superalloys, SAE Tech. Pap. 690102 (1969). doi:10.4271/690102.

[29] M. Vural, A. Akkuş, B. Eryürek, Effect of welding nugget diameter on the fatigue strength of the resistance spot welded joints of different steel sheets, J. Mater. Process. Technol. 176 (2006) 127–132. doi:10.1016/j.jmatprotec.2006.02.026.

[30] M. Vural, A. Akkus, On the resistance spot weldability of galvanized interstitial free steel sheets with austenitic stainless steel sheets, J. Mater. Process. Technol. 153-154 (2004) 1–6. doi:10.1016/j.jmatprotec.2004.04.063.

[31] S. Fatima, M. Khan, S.H.I. Jaffery, L. Ali, M. Mujahid, S.I. Butt, Optimization of process parameters for plasma arc welding of austenitic stainless steel (304 L) with low carbon steel (A-36), Proc. Inst. Mech. Eng. Part L J. Mater. Des. Appl. 230 (2016) 640–653. doi:10.1177/1464420715584392.

[32] D. Özyürek, An effect of weld current and weld atmosphere on the resistance spot weldability of 304L austenitic stainless steel, Mater. Des. 29 (2008) 597–603. doi:10.1016/j.matdes.2007.03.008.

[33] M. Zhou, S. Hu, H. Zhang, Critical specimen sizes for tensile-shear testing of steel sheets, Weld. J. 78 (1999) 305S–313S. http://aws.org/wj/supplement/sept99/ZHOU.pdf.

[34] Ó. Martín, V. Ahedo, J.I. Santos, P. De Tiedra, J.M. Galán, Quality assessment of resistance spot welding joints of AISI 304 stainless steel based on elastic nets, Mater. Sci. Eng. A. 676 (2016) 173–181. doi:10.1016/j.msea.2016.08.112.

[35] Ó. Martín, P. De Tiedra, M. López, M. San-Juan, C. García, F. Martín, Y. Blanco, Quality prediction of resistance spot welding joints of 304 austenitic stainless steel, Mater. Des. 30 (2009) 68–77. doi:10.1016/j.matdes.2008.04.050.

[36] ASTM E407-07e1, Standard Practice for Microetching Metals and Alloys, 2007.

[37] P. Marashi, M. Pouranvari, S. Amirabdollahian, A. Abedi, M. Goodarzi, Microstructure and failure behavior of dissimilar resistance spot welds between low carbon galvanized and austenitic stainless steels, Mater. Sci. Eng. A. 480 (2008) 175–180. doi:10.1016/j.msea.2007.07.007.

[38] ISO 14273, Specimen dimensions and procedure for shear testing resistance spot , seam and embossed projection welds, 2000.

[39] R.B. McCauley, M.P. Bennett, W.D. Bodary, G.C. Farrington, R.J. Gasser, W.W. Hurd, A.W. Schueler, T.W. Shearer, J.B. Silverberg, Resistance Spot Welding, in: T. Lyman (Ed.), Met. Handbook. Vol. 6 Weld. Brazing, 8th ed., American Society for Metals, Metals Park, OH, 1971: pp. 401–424.

[40] S. Aslanlar, The effect of nucleus size on mechanical properties in electrical resistance spot welding of sheets used in automotive industry, Mater. Des. 27 (2006) 125–131. doi:10.1016/j.matdes.2004.09.025.

[41] A. Hasanbasoglu, R. Kacar, Resistance spot weldability of dissimilar materials (AISI 316L-DIN EN 10130-99 steels), Mater. Des. 28 (2007) 1794–1800. doi:10.1016/j.matdes.2006.05.013.

[42] J.P. Kong, T.K. Han, K.G. Chin, B.G. Park, C.Y. Kang, Effect of boron content and welding current on the mechanical properties of electrical resistance spot welds in complex-phase steels, Mater. Des. 54 (2014) 598–609. doi:10.1016/j.matdes.2013.08.098.

[43] R. Raoelison, A. Fuentes, P. Rogeon, P. Carré, T. Loulou, D. Carron, F. Dechalotte, Contact conditions on nugget development during resistance spot welding of Zn coated steel sheets using rounded tip electrodes, J. Mater. Process. Technol. 212 (2012) 1663–1669. doi:10.1016/j.jmatprotec.2012.03.009.

[44] M. Zhou, H. Zhang, S.J. Hu, Relationships between quality and attributes of spot welds, Weld. J. 82 (2003) 72S–77S.

[45] J.M. Sawhill, J.C. Baker, Spot weldability of high-strength sheet steels, Weld. J. 59 (1980) 19S–30S.

[46] P. De Tiedra, Ó. Martín, M. San-Juan, Potentiodynamic study of the influence of gamma prime and eta phases on pitting corrosion of A286 superalloy, J. Alloys Compd. 673 (2016) 231–236. doi:10.1016/j.jallcom.2016.02.261.

[47] S.C. Ernst, W.A. Baeslack III, J.C. Lippold, Weldability of high-strength, low-expansion superalloys, Weld. J. 68 (1989) 418S–430S.

[48] Ó. Martín, P. De Tiedra, M. San-Juan, Study of influence of gamma prime and eta phases on corrosion behaviour of A286 superalloy by using electrochemical potentiokinetic techniques, Mater. Des. 87 (2015) 266–271. doi:10.1016/j.matdes.2015.08.041.

[49] S.H.I. Jaffery, P.T. Mativenga, Wear mechanisms analysis for turning Ti-6Al-4V—towards the development of suitable tool coatings, Int. J. Adv. Manuf. Technol. 58 (2012) 479–493. doi:10.1007/s00170-011-3427-y.

[50] Y.Z. Zhu, S.Z. Wang, B.L. Li, Z.M. Yin, Q. Wan, P. Liu, Grain growth and microstructure evolution based mechanical property predicted by a modified Hall-Petch equation in hot worked Ni76Cr19AlTiCo alloy, Mater. Des. 55 (2014) 456–462. doi:10.1016/j.matdes.2013.10.023.

[51] J.S. Van Sluytman, C.J. Moceri, T.M. Pollock, A Pt-modified Ni-base superalloy with high temperature precipitate stability, Mater. Sci. Eng. A. 639 (2015) 747–754. doi:10.1016/j.msea.2015.05.023.

[52] K. Kusabiraki, Y. Takasawa, T. Ooka, Precipitation and growth of γ′ and η Phases in 53Fe-26Ni-15Cr Alloy, ISIJ Int. 35 (1995) 542–547. doi:10.2355/isijinternational.35.542.

[53] Z. Zhong, Y. Gu, Y. Yuan, Microstructural stability and mechanical properties of a newly developed Ni-Fe-base superalloy, Mater. Sci. Eng. A. 622 (2015) 101–107. doi:10.1016/j.msea.2014.11.010.

[54] J.P. Shingledecker, N.D. Evans, G.M. Pharr, Influences of composition and grain size on creep-rupture behavior of Inconel® alloy 740, Mater. Sci. Eng. A. 578 (2013) 277–286. doi:10.1016/j.msea.2013.04.087.

[55] J.-C. Zhao, V. Ravikumar, A.M. Beltran, Phase precipitation and phase stability in nimonic 263, Metall. Mater. Trans. A. 32A (2001) 1271–1282. doi:10.1007/s11661-001-0217-4.

[56] S. Zhao, X. Xie, G.D. Smith, S.J. Patel, Research and Improvement on structure stability and corrosion resistance of nickel-base superalloy INCONEL alloy 740, Mater. Des. 27 (2006) 1120–1127. doi:10.1016/j.matdes.2005.03.015.

Figure Captions

Figure 1. (A) Diagram (not to scale) that shows the location of the area where the micrograph (B) was taken from the tensile shear test specimen; (B) SEM micrograph of a cross sectioned tensile shear test specimen that shows the weld nugget (WN) and the base metal (BM); (C) SEM micrograph of the as-cast dendritic microstructure of the weld nugget; (D) SEM micrograph of the base metal, which has polygonal austenitic grains. Electrolytic etching with etchant No. 83 according to ASTM E407-07 [36].

Figure 2. Load vs. displacement curves obtained from the tensile shear test performed on specimen No. 7 (precipitation hardening carried out at 720 °C for 0.5 h) and specimen No. 11 (precipitation hardening carried out at 720 °C for 100 h).

Figure 3. Experimental (exp) TSLBC, which was obtained in the tensile shear test, and predicted (pred) TSLBC [44,45] of each of the 13 tensile shear test specimens. Specimen No. 0 was subjected to no precipitation hardening treatment, i.e. it was in the solution treated (ST) condition and its aging time was considered as 0 h.

Figure 4. SEM micrograph of the weld nugget of the tensile shear test specimen No. 5. The arrow indicates the interdendritic region where the SEM/EDX analysis was performed. Electrolytic etching with etchant No. 83 according to ASTM E407-07 [36].

Figure 5. EDX spectrum obtained from the interdendritic región shown in Fig. 4.

Figure 6. SEM micrograph of the weld nugget of the tensile shear test specimen No. 10 where the inset provides the location of the studied zone. The γ' depleted zones in the dendrite core (DC) and the η phase at the interface between dendrite core and interdendritic region (IDR) are shown. Electrolytic etching with etchant No. 83 according to ASTM E407-07 [36].

Figure 7. Vickers hardness profile in the cross sectioned tensile shear test specimens No.7 and No. 11.

Figure 8. SEM micrographs that show Vickers indentations [49], performed on the cross sectioned tensile shear test specimens No.7 (bottom) and No. 11 (top). Electrolytic etching with etchant No. 83 according to ASTM E407-07 [36].

Figure 9. SEM micrograph of the base metal of the tensile shear test specimen No. 9 that shows the η phase precipitation at grain boundary. The inset provides a higher magnification image of the η phase. Electrolytic etching with etchant No. 83 according to ASTM E407-07 [36].

Figure 10. SEM micrograph of the base metal of the tensile shear test specimen No. 5 that shows the η phase precipitation at grain boundary. Electrolytic etching with etchant No. 83 according to ASTM E407-07 [36].

Figure 11. SEM micrograph of the weld nugget of the tensile shear test specimen No. 6 where there is no evidence of the presence of η phase. The inset provides a higher magnification image of the selected zone. Electrolytic etching with etchant No. 83 according to ASTM E407-07 [36].

Table Captions

Table 1. Chemical composition of A286 superalloy sheets (wt %).

Table 2. Tensile shear test specimens. Specimen No. 0 was subjected to no precipitation hardening treatment, i.e. it was in the solution treated condition. Each of different precipitation hardening treatments was followed by air cooling.

Table 3. Chemical composition (wt%) of interdendritic region determined by EDX and ratio k.